

中国激光

热处理对激光增材 ATI 718Plus 的组织与力学性能的影响

任逸群¹, 吴悦晨¹, 常帅¹, 李俐群^{1*}, 王民庆^{2**}

¹哈尔滨工业大学材料结构精密焊接与连接全国重点实验室, 黑龙江 哈尔滨 150001;

²钢铁研究总院, 北京 100081

摘要 使用激光熔化沉积技术制备了 ATI 718Plus 薄壁单墙样品, 研究了不同热处理工艺对沉积单墙组织及力学性能的影响。沉积态组织主要呈现外延生长的柱状树枝晶形貌, 枝晶间析出了大量 Laves 相, 该相消耗了大量的 Nb、Mo 等合金强化元素。试验发现热处理工艺对样品组织有着显著影响。直接时效热处理后, Laves 相未发生明显溶解, 但周围析出了大量的 η 相; 982 °C 固溶时效热处理后, Laves 相由长链状变为颗粒状, 有部分再结晶发生; 而 1020 °C 固溶时效热处理后, Laves 相基本溶解, 再结晶现象显著, 柱状晶转变为等轴晶。室温拉伸结果表明, 合适的热处理可以减少 Laves 相, 从而提高沉积样品的强度和塑性。其中直接时效热处理的强度最高, 相比沉积态抗拉强度提高了 51.9%, 但断后伸长率下降了 13%。1020 °C 固溶时效热处理的综合性能最好, 相比沉积态抗拉强度提高了 34.2%, 断后伸长率提高了 25.8%。

关键词 激光技术; 激光熔化沉积; 镍基高温合金; 热处理

中图分类号 TG456.7 文献标志码 A

DOI: 10.3788/CJL231244

1 引言

镍基高温合金因其良好的力学性能和耐腐蚀性能, 被广泛用于现代航空发动机、燃气轮机的制造^[1-2]。其中, ATI 718Plus 是近年来基于 IN718 开发的一种新型的镍基变形高温合金, 其服役温度为 704 °C^[3-4]。与 IN718 相比, ATI 718Plus 调整了 Al、Ti、Nb 等合金元素的含量, 主要强化相由 γ'' 相变为 γ' 相^[5], 晶界析出相由 δ 相变为 η 相, 故 650 °C 以上的热稳定性显著提高, 填补了 650 °C 用 IN718 和 750 °C 用 Waspaloy 合金之间长期存在的空白^[6]。并且 ATI 718Plus 兼具了 IN718 良好的综合力学性能、热加工和焊接性以及 Waspaloy 合金服役温度高的优点, 因而被认为是“下一代 IN718 合金”, 在航空发动机和燃气轮机领域中具有广阔的应用前景^[7]。

激光熔化沉积(LMD)技术是一种新型的增材制造技术^[8-9], 该技术使用粉末作为原材料, 基于三维数模可以实现复杂零件的近净成形, 节约材料的同时缩短生产周期, 降低成本, 适用于航空发动机叶片的修复与再制造^[10-11]。但由于激光熔化沉积快冷、反复加热冷却的特点, 镍基合金增材后的组织往往与锻态组织存在较大差异, 如增材样品由强<001>取向的柱状树

枝晶构成^[12-13]、枝晶间 Nb 元素富集导致出现了脆性相 Laves 相^[10, 14]。目前国内外学者对锻态 ATI 718Plus 的热处理制度及力学性能等进行了大量的研究^[15-17]。Wang 等^[3]发现, 适当含量的 η 相可以提高锻态 ATI 718Plus 的力学性能并降低缺口敏感性。Li 等^[18]研究了时效热处理时间对锻态 η 相演变和 700 °C 拉伸性能的影响。目前关于激光增材制造 ATI 718Plus 的组织和性能方面的研究则鲜有报道。

本文使用粉基激光熔化沉积法制备了 ATI 718Plus 样品, 重点研究了三种热处理制度(直接时效热处理制度、982 °C 固溶时效热处理制度和 1020 °C 高温固溶时效热处理制度)对 ATI 718Plus 微观组织演变、硬度以及室温拉伸性能的影响规律, 阐明了不同热处理制度下激光增材 ATI 718Plus 的相转变行为及力学性能变化, 以期为激光增材制造 ATI 718Plus 热处理工艺的选择提供指导。

2 试验方法

试验粉末为真空雾化的 ATI 718Plus 粉末, 图 1 所示为粉末的扫描电镜(SEM)形貌, 粉末粒径为 45~105 μm , 测定的粉末成分如表 1 所示。沉积基板为 ATI 718Plus 板材。试验开始前将粉末在 110 °C 真空

收稿日期: 2023-10-07; 修回日期: 2023-11-01; 录用日期: 2023-11-06; 网络首发日期: 2023-11-17

基金项目: 国家科技重大专项(J2019-VII-0004-0144)

通信作者: *Liliqun@hit.edu.cn; **minqingw@aliyun.com

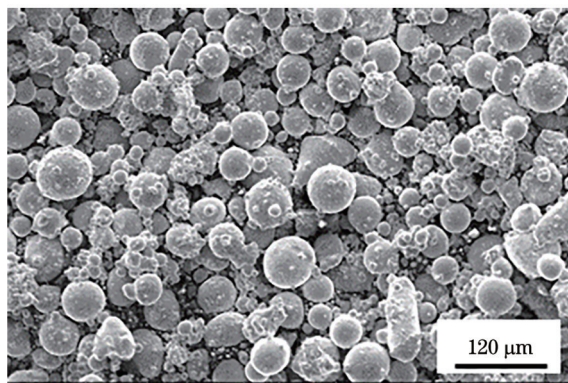


图 1 ATI 718Plus 粉末 SEM 形貌

Fig. 1 SEM morphology of ATI 718Plus powder

表 1 ATI 718Plus 粉末的化学成分(质量分数, %)

Table 1 Chemical compositions of ATI 718Plus powder (mass fraction, %)

Ni	Cr	Fe	Al	Co	Ti	Nb	Mo
50.87	18.72	9.56	2.29	8.40	0.71	4.35	3.57
52.00	18.80	9.32	2.32	8.86	0.86	3.98	2.49
51.59	18.10	9.26	1.27	8.61	0.98	5.53	3.06

干燥箱里烘干 40 min。

图 2(a) 为激光熔化沉积示意图, 激光光斑直径为 2 mm, 采用双筒送粉器, 整个熔覆过程在充氩仓内进

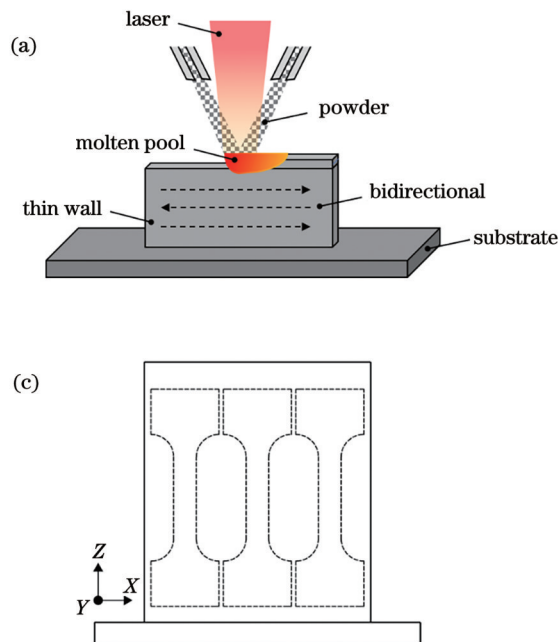


图 2 试验条件。(a) 激光熔化沉积设备示意图; (b) 热处理制度; (c) 拉伸样品取样位置; (d) 拉伸样品尺寸示意图

Fig. 2 Experimental conditions. (a) Schematic of LMD equipment; (b) heat treatment regime; (c) sampling position of tensile specimen; (d) tensile specimen size

3 分析与讨论

3.1 沉积态 ATI 718Plus 的微观组织特征

图 3 为沉积态样品的整体形貌及微观组织。图 3(a) 显示层间与道间的界面清晰可见, 无明显裂纹、气孔及

未熔合等缺陷。沉积态样品内为沿基材向沉积方向外延生长的柱状树枝晶组织, 且柱状晶能穿越多层沉积层, 这是激光增材制造快速冷却、凝固的特点引起的典型微观组织特征。由于最大冷却速度方向与沉积方向并非完全一致, 故柱状晶生长方向略微偏向激

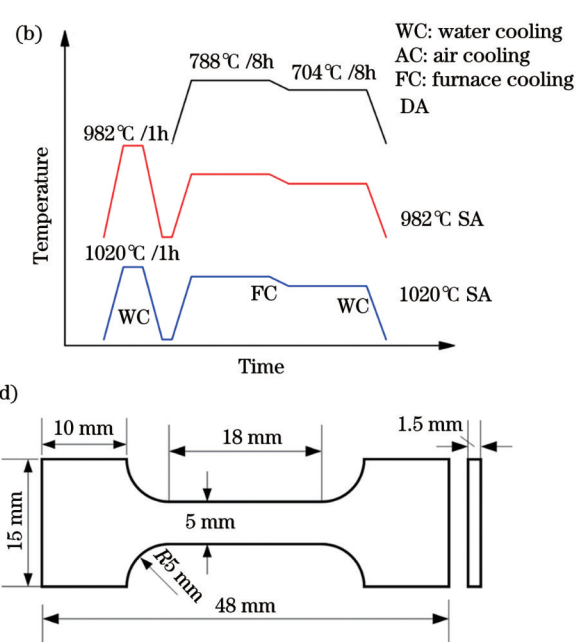


图 2 试验条件。(a) 激光熔化沉积设备示意图; (b) 热处理制度; (c) 拉伸样品取样位置; (d) 拉伸样品尺寸示意图

Fig. 2 Experimental conditions. (a) Schematic of LMD equipment; (b) heat treatment regime; (c) sampling position of tensile specimen; (d) tensile specimen size

未熔合等缺陷。沉积态样品内为沿基材向沉积方向外延生长的柱状树枝晶组织, 且柱状晶能穿越多层沉积层, 这是激光增材制造快速冷却、凝固的特点引起的典型微观组织特征。由于最大冷却速度方向与沉积方向并非完全一致, 故柱状晶生长方向略微偏向激

光扫描方向。熔池在前进过程中,除了向前一层散热外还可以向同层已成形的部分散热,散热最快的方向并不是垂直向下而是与前进方向相反的斜向下,最终使得晶体生长有如此倾斜的取向^[20]。层间与道间界面在光镜下表现为白色带状区。采用 SEM 放大观察,如图 3(b)所示,该处 Laves 相显得更加连续且密集。图 3(c)展示了 XY 面的枝晶形貌,发现枝晶横断面呈现十字形,枝晶核粗细均匀。沉积区表现出典型的细长枝晶结构,如图 3(d)所示,枝晶核处深色相为 γ 基体,而细长的不规则白色相为枝晶间 Laves 相,且二次枝晶臂不发达。LMD 快速冷却的特点导致 ATI 718Plus 在熔池固液界面处产生严重的枝晶间元素偏析,在凝固的最后阶段通过共晶 Laves/ γ 反应,形成脆性金属间化合物 Laves 相^[21]。图 3(e)展示了 Laves 相

在沉积区的高倍形态,既存在连续的长链状,也存在间断的颗粒状,但长链状 Laves 相占多数。图 3(f)和表 2 为枝晶不同位置的能谱(EDS)测试结果,可以发现枝晶间区域富集了大量 Nb、Mo 等元素。Nb、Mo 这两种元素在镍基合金凝固过程中的再分配系数 $k < 1$,在凝固过程中容易在残余液相处富集。Dupont 等^[22-23]发现,一旦液相中 Nb 元素的含量(质量分数)大于 23.1%,则会产生 Laves 相。通常认为,Laves 是一种硬脆相,其与基体无法协同变形,从而导致裂纹的萌生和扩展^[24]。而且 Nb 等元素的偏析使得 γ 基体缺少析出强化相所需要的合金元素,而 Mo 等元素的偏析导致合金固溶强化的效果降低,因而 Laves 相通常被认为是有害相,它会削弱沉积态镍基高温合金的力学性能^[25-27]。

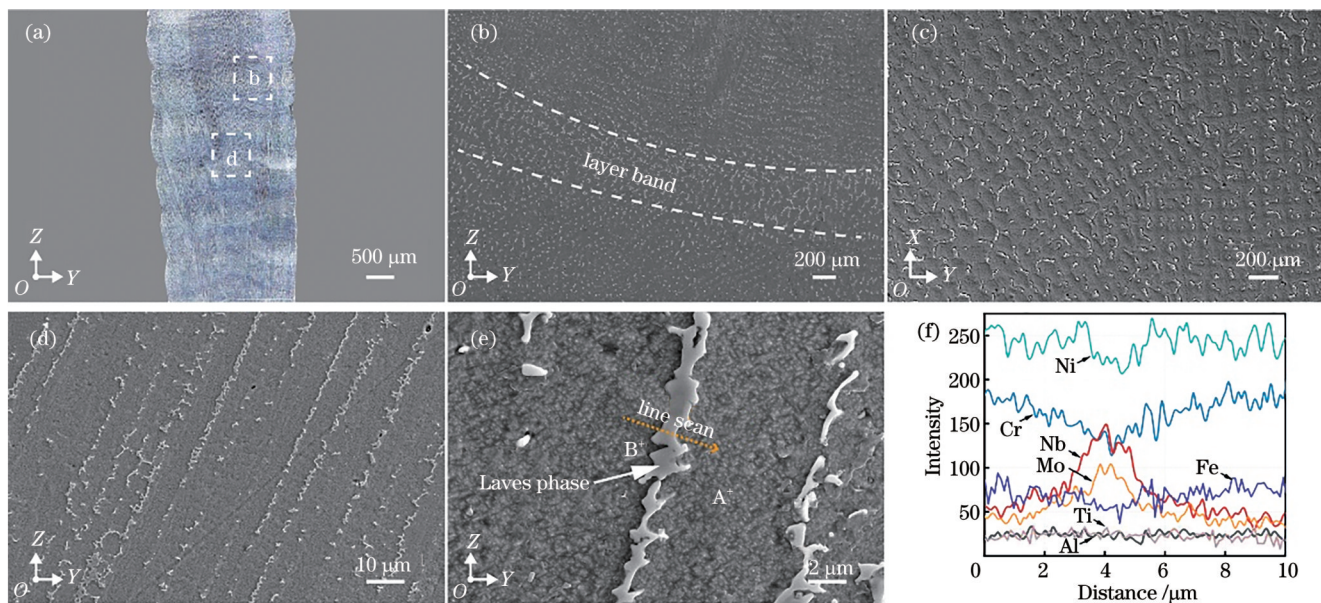


图 3 沉积态样品组织。(a) XZ 面的宏观形貌;(b)层带处的 SEM 形貌;(c) XY 面的枝晶形貌;(d) XZ 面的组织形貌;(e) Laves 相;(f)元素线分布

Fig. 3 Microstructures of as-deposited sample. (a) Macroscopic morphology of XZ surface; (b) SEM morphology at layer band; (c) dendritic morphology of XY plane; (d) microstructure of XZ plane; (e) Laves phase; (f) element line distribution

表 2 枝晶间和枝晶核位置的元素成分(质量分数, %)

Table 2 Elemental compositions of inter-dendrite region and dendrite core (mass fraction, %)

Position	Ni	Cr	Fe	Al	Co	Ti	Nb	Mo
Dendrite core (point A)	53.34	19.42	9.89	1.76	9.01	0.54	3.14	2.9
Inter-dendrite region (point B)	51.19	18.2	9.34	1.53	8.91	1.43	6.93	2.47

3.2 热处理后 ATI 718Plus 的微观组织特征

图 4 为经过直接时效处理后样品的微观组织。总体来看,样品枝晶形貌没有明显变化,仍然由柱状树枝晶构成[图 4(a)]。枝晶间 Laves 相仍然为长链状,这是因为直接时效的热处理温度远远低于 Laves 相的溶解温度(约为 1165 °C^[28]),无法促使 Laves 相发生大量溶解。除此之外,时效热处理后样品中新析出了针状 η 相和 γ' 相。但值得注意的是,针状 η 相和 γ' 相均在

枝晶间析出较多。如图 4(d)所示, γ' 相在枝晶间的分布更为密集,在枝晶核则析出较少,而针状 η 相则基本都在枝晶间 Laves 相周围析出。 η 相是 ATI 718Plus 中常见的析出相,其成分为 Ni_6AlNb ^[7],而 γ' 相为 ATI 718Plus 的主要强化相,其成分为 $Ni_3(Al, Ti, Nb)$ 。由此可见,Nb 元素是形成这两种第二相的重要元素^[15]。据文献^[29]报道,枝晶间的 Nb、Mo 和 Ti 含量的增加会加速镍基合金中第二相的沉淀。为证明元素偏析对 η

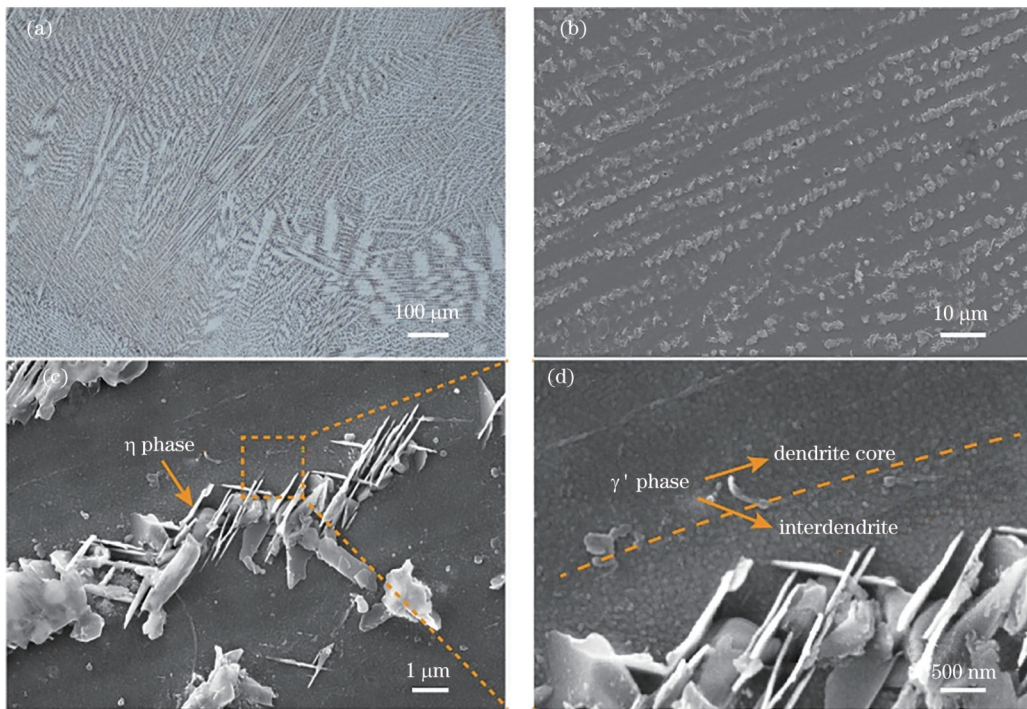


图 4 DA 样品在 XZ 面的微观组织。(a) 宏观形貌; (b)~(d)SEM 微观组织

Fig. 4 Microstructures of DA sample in XZ plane. (a) Macro-morphology; (b)–(d) SEM morphologies

相和 γ' 相析出的影响,基于表2枝晶间和枝晶核位置的元素成分,使用JMatpro计算得到了ATI 718Plus的

等温转变曲线(图5),枝晶间的 η 相和 γ' 相均比枝晶核的 η 相和 γ' 相析出提前。

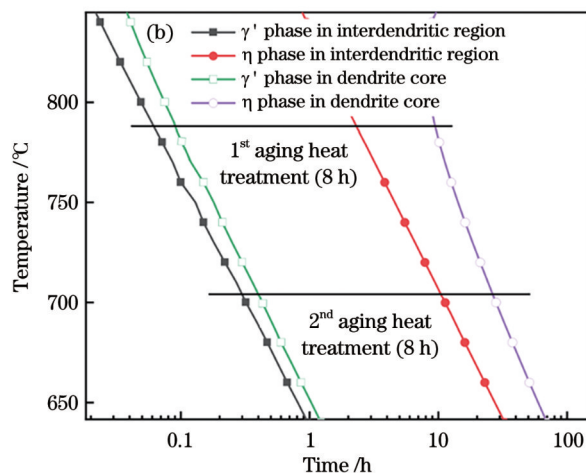
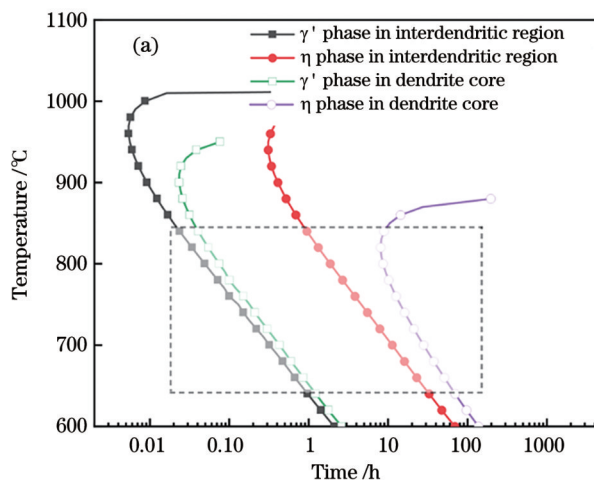


图 5 由 JMatPro 计算得到的枝晶间与枝晶核的 TTT 曲线。(a) TTT 曲线;(b)局部放大图

Fig. 5 TTT curves of inter-dendritic region and dendrite core calculated by JMatPro. (a) TTT curve; (b) partial magnification

图6为982 °C固溶时效热处理后样品的组织形貌。与直接时效的样品相比,由于982 °C的热处理温度接近镍基合金的完全再结晶温度1100 °C,而且增材修复后样品内的残余应力较大,再结晶驱动力强,因此样品的枝晶特征减弱,有部分柱状树枝晶发生再结晶,出现了新的晶界。如图6(b)所示,长链状Laves相部分溶解,变为颗粒状Laves相。高倍SEM图像显示 γ' 相基本在整个枝晶区域内均匀分布,但仍有部分短针状 η 相在Laves相周围析出,这是因为Nb元素在镍基合金 γ 基体中的扩散速率较慢,尽管在时效热处理前经过

了982 °C固溶处理,但Nb元素的扩散距离和迁移程度仍不够,Nb元素在枝晶间的偏聚仍然存在。

经过更高温度(1020 °C)的固溶时效处理后样品元素偏析基本消除,如图7所示,增材样品原有的枝晶形貌基本消失,沉积态的柱状树枝晶被再结晶后的等轴晶替代。长链状Laves相基本溶解,仅剩下少量离散分布的小颗粒状Laves相。高倍SEM图像[图7(c)]显示,Laves相尺寸大大减小,只有少量 η 相, γ' 相分布均匀。

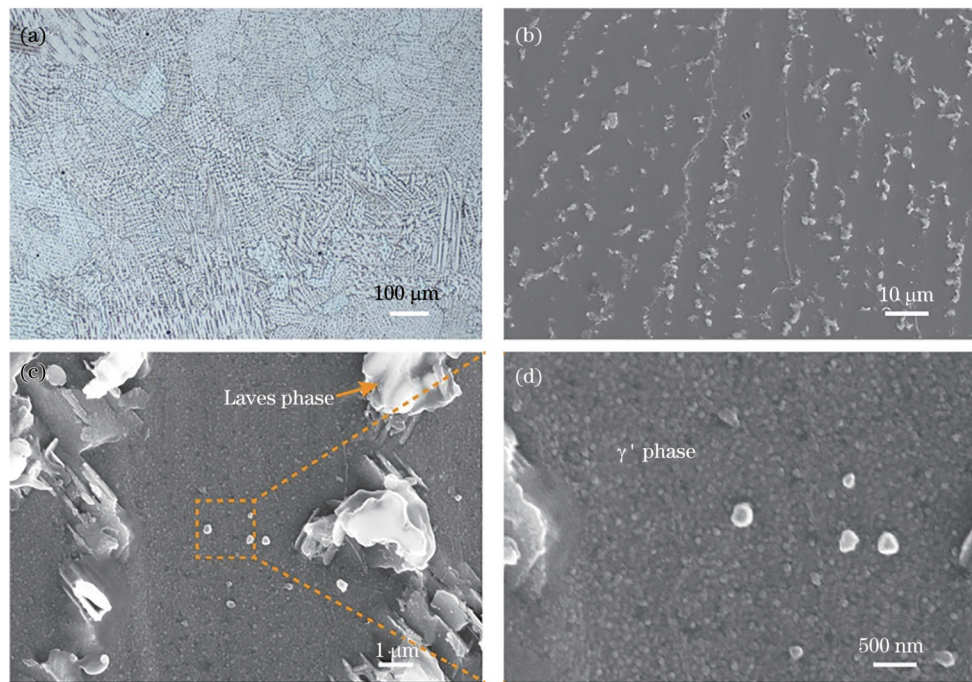


图 6 982 °C SA 样品 XZ 面的微观组织。(a)宏观形貌;(b)~(d)SEM 微观组织

Fig. 6 Microstructures of 982 °C SA sample in XZ plane. (a) Macro-morphology; (b)–(d) SEM morphologies

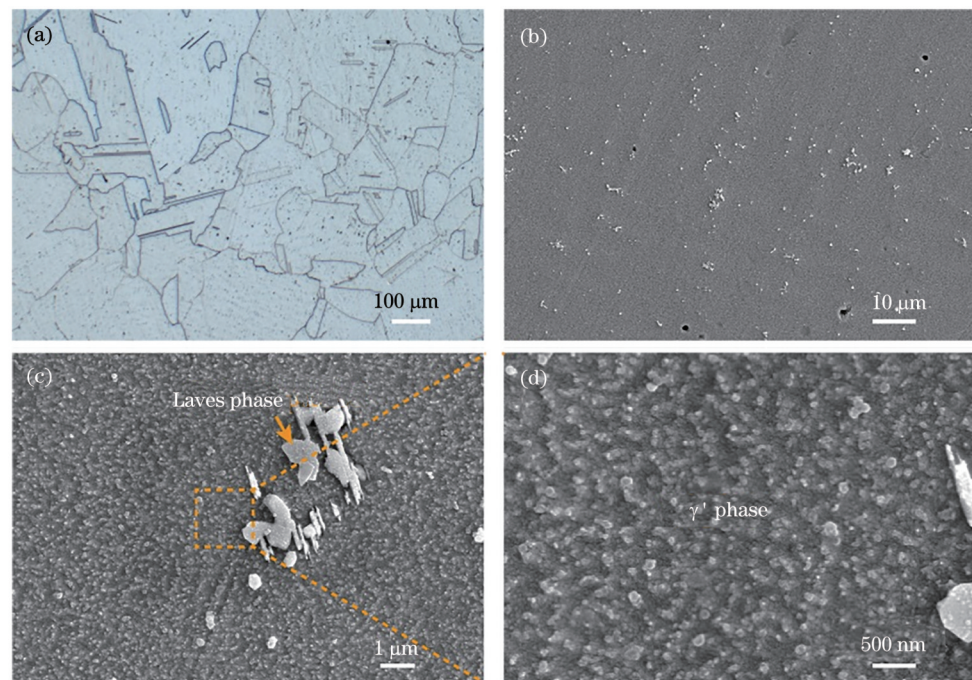


图 7 1020 °C SA 样品 XZ 面的微观组织。(a)宏观形貌;(b)~(d)SEM 微观组织

Fig. 7 Microstructures of 1020 °C SA sample in XZ plane. (a) Macro-morphology; (b)–(d) SEM morphologies

3.3 沉积态及热处理态增材件的力学性能

激光熔化沉积制造的 ATI 718Plus 沉积态样品及不同热处理后样品的硬度如表 3 所示。与沉积态相比,热处理后样品硬度有显著提升,其中直接时效热处理后样品硬度提升了 32.4%,但三种热处理样品之间的硬度差异较小。

激光熔化沉积制造的 ATI 718Plus 沉积态样品及不同热处理后样品的室温拉伸性能如图 8 所示。与沉

表 3 沉积态及不同热处理样品的硬度

Table 3 Hardness values of as-deposited sample and samples after different heat treatments

Heat treatment regime	Hardness /HV
As-deposited sample	338.5
DA sample	457.2
982 °C SA sample	447.9
1020 °C SA sample	466.4

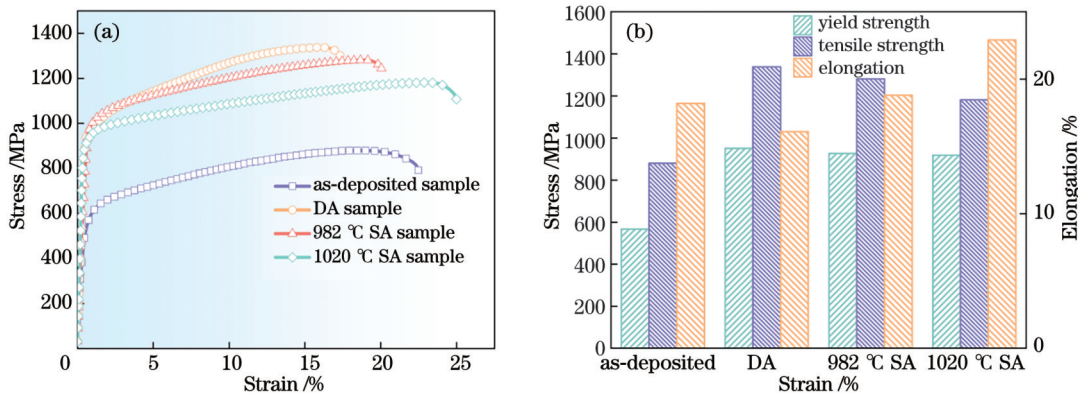


图 8 沉积态及不同热处理样品的拉伸性能。(a)拉伸曲线;(b)拉伸结果柱状图

Fig. 8 Tensile properties of as-deposited sample and samples after different heat treatments. (a) Tensile curves; (b) histogram of tensile results

积态样品相比,热处理后的样品无论是屈服强度还是抗拉强度都有显著提升,但断后伸长率先减小后增大。直接时效热处理后屈服强度提升了67.7%,抗拉强度提升了51.9%,同时断后伸长率降低了13%;982 °C固溶时效热处理后,尽管强度提升不如直接时效热处理,但是屈服强度仍然提升了63.6%,抗拉强度提升了45.6%。断后伸长率相比沉积态提升了3%;1020 °C高温固溶时效热处理后,强度提升最少,屈服强度仅提升62.0%,抗拉强度提升了34.2%,但塑性得到明显改

善,断后伸长率相比沉积态提升了25.8%。

图9为沉积态和不同热处理后样品的断口形貌。断口表现出典型的微孔聚集型断裂模式^[25],为韧性断裂。根据韧窝排布特征,断口形貌可以分为两类。(i)沉积态、直接时效、982 °C固溶时效样品的韧窝表现出成行成列整齐排列的特点,这与图3(c)中XY平面的枝晶形貌相似。分别对沉积态样品断口的撕裂棱区域area 1和韧窝内部夹杂物区域area 2进行EDS测试,结果如表4所示。韧窝内部的小颗粒富含大量的Nb元

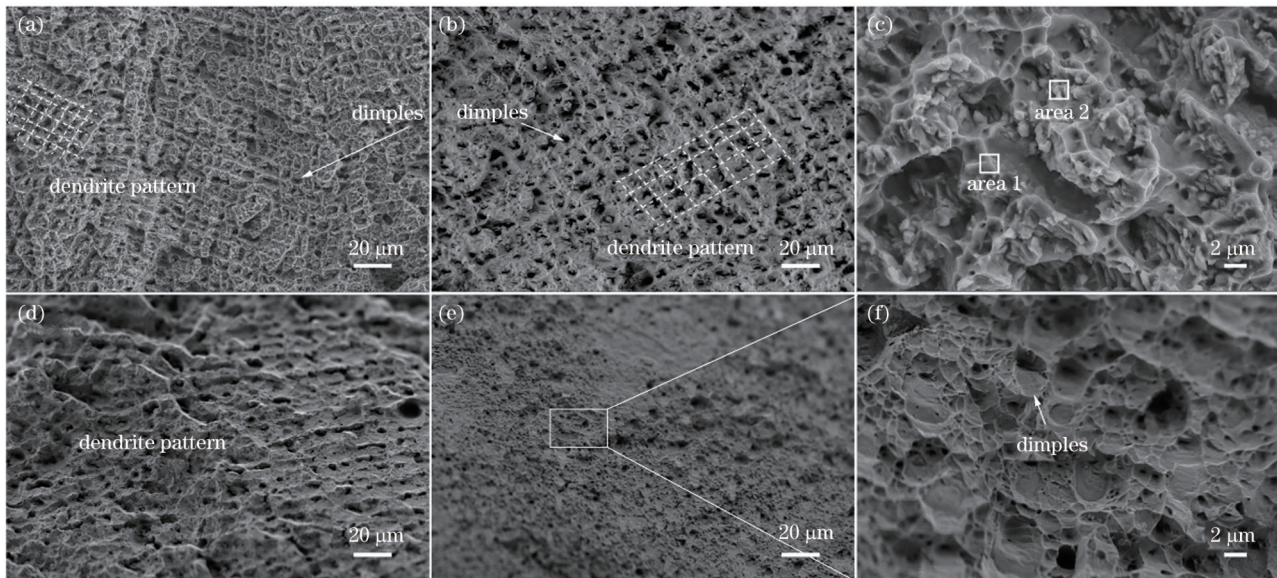


图9 沉积态及不同热处理样品的断口形貌。(a)沉积态样品;(b) DA 样品;(c)沉积态样品断口的高倍形貌;(d) 982 °C SA 样品;(e) 1020 °C SA 样品;(f) 1020 °C SA 样品断口的高倍形貌

Fig. 9 Fracture morphologies of as-deposited sample and samples after different heat treatments. (a) As-deposited sample; (b) DA sample; (c) high magnification morphology of as-deposited sample fracture; (d) 982 °C SA sample; (e) 1020 °C SA sample; (f) high magnification morphology of 1020 °C SA sample fracture

表4 沉积态样品断口区域的元素成分(质量分数, %)

Table 4 Element compositions of as-deposited sample fracture area (mass fraction, %)

Area	Al	Ti	Nb	Mo	Cr	Fe	Co	Ni
Area 1	1.75	0.89	5.00	2.79	19.05	9.94	9.29	Bal.
Area 2	2.19	1.02	14.80	3.83	15.54	7.77	8.74	Bal.

素,而撕裂棱缺少 Nb 元素,结合图 3(c)推断,韧窝内部夹杂为 Laves 相。Laves 相是镍基合金中常见的一种硬脆相,当基体发生塑性变形时,长链状的 Laves 相与基体协同变形的能力较差^[30],裂纹容易在 Laves 相周围萌生,并形成微孔,而由于 Laves 相倾向于在枝晶间形成,因而其分布导致断口表现出枝晶生长特征^[27,31]。(ii) 1020 °C 高温固溶时效处理的样品韧窝排列没有明显的倾向性,断口由大韧窝和小韧窝组成,小韧窝分布在大韧窝侧壁上。这是因为经过 1020 °C 高温固溶时效热处理后,Laves 相显著溶解。Sui 等^[32]研究发现,小颗粒 Laves 相与基体协同变形的能力提高,Laves 相与基体界面位置的应力集中减少,不再成为裂纹产生的主要诱因。

3.4 热处理对组织性能的影响

试验结果表明,激光熔化沉积制备的 ATI 718Plus 的元素偏聚严重,大量的 Nb、Mo 等元素聚集在枝晶间,这种元素偏聚使得后续热处理制度的选择对增材制造的 ATI 718Plus 尤为重要。1) 经过热处理后样品硬度与强度显著提高。ATI 718Plus 是一种主要由 γ' 相沉淀强化的镍基高温合金。由于激光快冷非平衡凝固的特点, γ' 相来不及析出。且凝固过程中 Nb、Mo 元素容易偏聚在枝晶间,导致了 Laves 相的析出^[33],该相的形成消耗掉了大量的 Nb 合金元素,进一步抑制了 $\gamma'-\text{Ni}_3(\text{Al}, \text{Ti}, \text{Nb})$ 相的析出,降低了沉淀强化作用。而经过后续热处理后,一方面 Laves 相溶解,有利的合金元素扩散到基体中;另一方面, γ' 相经过时效保温热处理后析出^[34],从而提高了样品性能。2) 随热处理温度的提高,样品塑性显著提高。这是因为直接时效热处理后,长链状的 Laves 未发生溶解,且在 Laves 周围析出了大量的针状 η 相。前文提到长链状的 Laves 相是裂纹产生的主要原因,而大量析出的针状 η 相会构成魏氏组织^[35],进一步阻碍位错移动,降低塑性。因此,直接时效样品的塑性最差。而经过固溶时效热处理后,无论是 Laves 相还是 η 相尺寸都逐渐减小,含量降低,塑性得以大幅提高。

4 结 论

研究了沉积态和不同热处理制度后激光熔化沉积 ATI 718Plus 的微观组织的演变规律,并对平行建造方向的力学性能进行测试分析,主要得到了以下结论:

1) 沉积态的样品主要呈现外延生长的柱状树枝晶形貌,枝晶间析出了大量长链状 Laves 相,该相为脆性相,并且消耗了大量的 Nb、Mo 等强化元素,严重降低了沉积态样品的力学性能。

2) 直接时效热处理后长链状 Laves 相形貌未发生明显变化,且 η 相和 γ' 相在枝晶间大量析出。固溶时效热处理制度可以有效减小 Laves 相的尺寸和含量。随着固溶温度的提高,Laves 相和 η 相的尺寸和含量逐渐减小, γ' 相均匀析出。

3) 热处理后 ATI 718Plus 增材样品的强度和硬度显著提高,1020 °C 高温固溶时效热处理后样品的强度和塑性匹配最佳。相比沉积态,1020 °C 固溶时效热处理样品的抗拉强度提升了 34.2%,断后伸长率提升了 25.8%。

参 考 文 献

- [1] Wang M Q, Deng Q, Du J H, et al. The effect of aluminum on microstructure and mechanical properties of ATI 718Plus alloy[J]. Materials Transactions, 2015, 56(5): 635-641.
- [2] Xie B C, Zhang B Y, Yu H, et al. Microstructure evolution and underlying mechanisms during the hot deformation of 718Plus superalloy[J]. Materials Science and Engineering: A, 2020, 784: 139334.
- [3] Wang M Q, Du J H, Deng Q, et al. Effect of the precipitation of the $\eta-\text{Ni}_3\text{Al}_{0.5}\text{Nb}_{0.5}$ phase on the microstructure and mechanical properties of ATI 718Plus[J]. Journal of Alloys and Compounds, 2017, 701: 635-644.
- [4] Kennedy R L. Allvac 718Plus, superalloy for the next forty years [EB/OL]. [2023-05-04]. https://www.tms.org/Superalloys/10.7449/2005/Superalloys_2005_1_14.pdf.
- [5] Guo Q Y, Ma Z Q, Qiao Z X, et al. A new type- γ'/γ coprecipitation behavior and its evolution mechanism in wrought Ni-based ATI 718Plus superalloy[J]. Journal of Materials Science & Technology, 2022, 119: 98-110.
- [6] Whitmore L, Ahmadi M R, Stockinger M, et al. Microstructural investigation of thermally aged nickel-based superalloy 718Plus[J]. Materials Science and Engineering: A, 2014, 594: 253-259.
- [7] Pickering E J, Mathur H, Bhowmik A, et al. Grain-boundary precipitation in Allvac 718Plus[J]. Acta Materialia, 2012, 60(6/7): 2757-2769.
- [8] 俞皓捷, 戴冬华, 石新宇, 等. 曲面激光增材制造钛/铝异质材料起始及稳态沉积过程热行为研究[J]. 中国激光, 2023, 50(8): 0802302.
- [9] Yu H J, Dai D H, Shi X Y, et al. Thermal behaviors of initial and steady state deposition processes of Ti/Al heterogeneous materials fabricated by laser additive manufacturing on curved surface[J]. Chinese Journal of Lasers, 2023, 50(8): 0802302.
- [10] 杨光, 邹文北, 王超, 等. 激光增材连接异质铝合金的组织及性能研究[J]. 中国激光, 2022, 49(22): 2202010.
- [11] Yang G, Zou W B, Wang C, et al. Microstructure and properties of laser additive jointing heterogeneous aluminum alloys[J]. Chinese Journal of Lasers, 2022, 49(22): 2202010.
- [12] Zhao J F, Cheng C, Xie D Q, et al. High-temperature tensile property of GH4169 nickel-based superalloys by laser repair[J]. Chinese Journal of Lasers, 2016, 43(8): 0802012.
- [13] 威永爱, 赵剑峰, 谢德巧, 等. 激光修复 GH4169 镍基高温合金的弯曲性能[J]. 中国激光, 2013, 40(11): 1103009.
- [14] Qi Y A, Zhao J F, Xie D Q, et al. Flexural property of GH4169 nickel-based superalloy by laser repair[J]. Chinese Journal of Lasers, 2013, 40(11): 1103009.
- [15] 于群, 王存山, 董闯. 激光增材制造 Ni-Cr-Al 基础合金系组织与性能研究[J]. 中国激光, 2022, 49(14): 1402104.
- [16] Yu Q, Wang C S, Dong C. Microstructure and properties of Ni-Cr-Al basic alloys fabricated by laser additive manufacturing[J]. Chinese Journal of Lasers, 2022, 49(14): 1402104.
- [17] Zhang Y C, Yang L, Lu W Z, et al. Microstructure and elevated temperature mechanical properties of IN718 alloy fabricated by laser metal deposition[J]. Materials Science and Engineering: A, 2020, 771: 138580.
- [18] Marchese G, Lorusso M, Parizia S, et al. Influence of heat treatments on microstructure evolution and mechanical properties

- of Inconel 625 processed by laser powder bed fusion[J]. Materials Science and Engineering: A, 2018, 729: 64-75.
- [15] Tang L T, Zhang H Y, Guo Q Y, et al. The precipitation of η phase during the solution treatments of Allvac 718Plus[J]. Materials Characterization, 2021, 176: 111142.
- [16] Li J, Ding R, Guo Q Y, et al. Effect of solution cooling rate on microstructure evolution and mechanical properties of Ni-based superalloy ATI 718Plus[J]. Materials Science and Engineering: A, 2021, 812: 141113.
- [17] Qi Q Q, Zhang H J, Liu C X, et al. On the microstructure evolution during low cycle fatigue deformation of wrought ATI 718Plus alloy[J]. Materials Science and Engineering: A, 2020, 798: 140132.
- [18] Li J, Wu Y T, Liu Y C, et al. Enhancing tensile properties of wrought Ni-based superalloy ATI 718Plus at elevated temperature via morphology control of η phase[J]. Materials Characterization, 2020, 169: 110547.
- [19] Srinivasan D, Lawless L U, Ott E A. Experimental determination of TTT diagram for alloy 718Plus®[M]. Singapore: John Wiley & Sons, Inc., 2012: 759-68.
- [20] Dinda G P, Dasgupta A K, Mazumder J. Texture control during laser deposition of nickel-based superalloy[J]. Scripta Materialia, 2012, 67(5): 503-506.
- [21] Kermanpur A, Babu R P, Larsson H, et al. Simulation and experimental analysis of nanoscale precipitation during ageing treatment of laser powder-bed fusion fabricated IN718 Ni-based superalloy[J]. Materials Characterization, 2022, 191: 112163.
- [22] DuPont J N, Marder A R, Notis M R, et al. Solidification of Nb-bearing superalloys: part II. pseudoternary solidification surfaces[J]. Metallurgical and Materials Transactions A, 1998, 29(11): 2797-2806.
- [23] DuPont J N, Notis M R, Marder A R, et al. Solidification of Nb-bearing superalloys: part I. reaction sequences[J]. Metallurgical and Materials Transactions A, 1998, 29(11): 2785-2796.
- [24] Sui S, Chen J, Zhang R, et al. The tensile deformation behavior of laser repaired Inconel 718 with a non-uniform microstructure[J]. Materials Science and Engineering: A, 2017, 688: 480-487.
- [25] Sui S, Chen J, Ming X L, et al. The failure mechanism of 50% laser additive manufactured Inconel 718 and the deformation behavior of Laves phases during a tensile process[J]. The International Journal of Advanced Manufacturing Technology, 2017, 91(5): 2733-2740.
- [26] Yuan K B, Guo W G, Li P H, et al. Influence of process parameters and heat treatments on the microstructures and dynamic mechanical behaviors of Inconel 718 superalloy manufactured by laser metal deposition[J]. Materials Science and Engineering: A, 2018, 721: 215-225.
- [27] Sui S, Chen J, Ma L, et al. Microstructures and stress rupture properties of pulse laser repaired Inconel 718 superalloy after different heat treatments[J]. Journal of Alloys and Compounds, 2019, 770: 125-135.
- [28] Li X, Shi J J, Wang C H, et al. Effect of heat treatment on microstructure evolution of Inconel 718 alloy fabricated by selective laser melting[J]. Journal of Alloys and Compounds, 2018, 764: 639-649.
- [29] Jang J, Yim J, Lee S H. Phase formation kinetics during heat treatments of Inconel 718 deposits based on cold metal transfer-based wire arc additive manufacturing[J]. Materials Characterization, 2022, 193: 112294.
- [30] Asala G, Andersson J, Ojo O A. Improved dynamic impact behaviour of wire-arc additive manufactured ATI 718Plus®[J]. Materials Science and Engineering: A, 2018, 738: 111-124.
- [31] Sui S, Zhong C L, Chen J, et al. Influence of solution heat treatment on microstructure and tensile properties of Inconel 718 formed by high-deposition-rate laser metal deposition[J]. Journal of Alloys and Compounds, 2018, 740: 389-399.
- [32] Sui S, Tan H, Chen J, et al. The influence of Laves phases on the room temperature tensile properties of Inconel 718 fabricated by powder feeding laser additive manufacturing[J]. Acta Materialia, 2019, 164: 413-427.
- [33] Hu Y L, Lin X, Li Y L, et al. Influence of heat treatments on the microstructure and mechanical properties of Inconel 625 fabricated by directed energy deposition[J]. Materials Science and Engineering: A, 2021, 817: 141309.
- [34] Zhang S Y, Lin X, Wang L L, et al. Strengthening mechanisms in selective laser-melted Inconel718 superalloy[J]. Materials Science and Engineering: A, 2021, 812: 141145.
- [35] Chen Y H, Yang C L, Fan C L, et al. The influence of solution temperature on microstructure evolution and mechanical properties of ATI 718Plus repaired by wire and arc additive manufacturing[J]. Materials Science and Engineering: A, 2022, 852: 143641.

Effects of Heat Treatment on Microstructure and Mechanical Property of ATI 718Plus by Laser Additive Manufacturing

Ren Yiqun¹, Wu Yuechen¹, Chang Shuai¹, Li Liquin^{1*}, Wang Minqing^{2**}

¹State Key Laboratory of Advanced Welding and Joining, Harbin Institute of Technology, Harbin 150001, Heilongjiang, China;

²Central Iron & Steel Research Institute, Beijing 100081, China

Abstract

Objective Laser melting deposition is used to prepare ATI 718Plus samples to study the effects of three heat treatment regimes on their microstructure evolution, hardness, and room temperature tensile properties. These regimes include direct aging heat treatment, solutionizing and aging heat treatment at 982 °C, and high-temperature solutionizing and aging heat treatment at 1020 °C. The aim is to elucidate the phase transformation behavior and mechanical property changes of laser additive ATI 718Plus under different heat treatment regimes and provide guidance for the selection of heat treatment processes used in the laser additive manufacturing of ATI

718Plus.

Methods The plasma rotating electrode process is used with ATI 718Plus powder with particle diameter of 45–105 μm to prepare wrought ATI 718Plus superalloy substrates. The experiments are performed on the laser additive manufacturing system shown in Fig. 2, which consists of a 4000 W continuous wave fiber laser, an inert atmosphere processing chamber, a coaxial nozzle, and a powder feeding device. A well-formed ATI 718Plus sample is prepared using a unidirectional reciprocating scanning method with the following parameters: a laser power of 1200 W, scanning speed of 0.8 m/min, protective gas flow rate of 10 L/min, carrier gas flow rate of 15 L/min, and powder feed rate of 13 g/min. The geometric dimensions of each sample are 50.0 mm \times 58.0 mm \times 2.5 mm. Three heat treatment regimes are employed, as shown in Fig. 2(b). The analyzed samples are mechanically ground with SiC paper and polished using diamond suspensions and a colloidal silica suspension to prepare metallurgical samples. Then, the polished samples are etched with No. 2 waterless Kailing's reagent for optical microscope and scanning electron microscope (SEM) investigations. Uniaxial tensile tests are carried out at room temperature using a universal testing machine with a constant displacement rate of 1 mm/min.

Results and Discussions After laser deposition, a large number of Laves phase areas form in the interdendritic region (Fig. 3). This hard and brittle phase deteriorates the mechanical properties of the additive-manufactured ATI 718Plus samples. The as-deposited sample mainly exhibits an epitaxial growth columnar dendritic morphology, with a large number of brittle long-chain Laves phases precipitated between dendrites, which consumes a significant amount of Nb, Mo, and other strengthening elements, severely reducing the mechanical properties of the as-deposited sample. After the direct aging heat treatment, the long-chain Laves phase morphology remains unchanged, and the η and γ' phases precipitate heavily between dendrites. The solution and aging heat treatment system can effectively reduce the size and content of the Laves phase. With an increase in the solution temperature, the size and content of the Laves and η phases gradually decrease, and the γ' phase uniformly precipitates. The hardness significantly increases after heat treatment (Table 2), but the hardness differences between the three heat treatments are relatively small. The room temperature tensile properties are shown in Fig. 8. Compared to the as-deposited sample, after heat treatment the samples exhibit significant increases in both the yield strength and tensile strength, while the elongation at fracture decreases and then increases. The yield and tensile strengths increase by 67.7% and 51.9% after the direct aging heat treatment, respectively, while the elongation at fracture decreases by 13%. After the solution aging (SA) heat treatment at 982 °C, although the strength improvement is not as significant as that after the direct aging treatment, the yield and tensile strengths still increase by 63.6% and 45.6%, respectively. At the same time, the elongation at fracture increases by 3% compared to that of the as-deposited state. The strength improvement is the smallest after the 1020 °C SA, with a yield strength increase of only 62.0% and tensile strength increase of 34.2%, but the plasticity is significantly improved, with an elongation at fracture increase of 25.8% compared to that of the as-deposited state.

Conclusions The strength and hardness values of the ATI 718Plus additive samples significantly increase after heat treatment. The best match between strength and plasticity is obtained after high-temperature solution and aging heat treatment at 1020 °C. Compared with those of the as-deposited state, the tensile strength and elongation at the fracture of the sample increase by 34.2% and 25.8%, respectively, after the 1020 °C solution and aging heat treatment.

Key words laser technique; laser melting deposition; nickel-based superalloy; heat treatment